OPTICS

Shortcuts to adiabatic non-Abelian braiding on silicon photonic chips

Wange Song[1,2]†, Xuanyu Liu[1]†, Jiacheng Sun[1]†, Oubo You[2], Shengjie Wu[1], Chen Chen[1], Shining Zhu[1], Tao Li[1]*, Shuang Zhang[2,3,4]*

Non-Abelian braiding describes the exchange behavior of anyons, useful for encoding qubits for quantum computing. Recently, this concept has been realized in classical photonic and acoustic systems. However, these implementations are constrained by adiabatic conditions, necessitating long operation distances and hindering practical applications. Here, we conceive and demonstrate shortcut to adiabatic (STA) braiding of light in three-dimensional silicon photonic chips. Our device comprises trilayer silicon waveguides embedded in the SU-8 polymer, using an STA strategy to expedite the braiding operations, resulting in compact devices that function as photonic quantum X, Y, and Z gates. We further experimentally observed non-Abelian braiding behaviors based on this STA-braiding scheme. Our work represents a compact braiding apparatus with a size reduction of nearly three orders of magnitude compared to previous works. This work presents a feasible approach to accelerating adiabatic braiding evolutions, paving the way for compact, CMOS-compatible non-Abelian photonic devices.

INTRODUCTION

Non-Abelian phenomena are pervasive and have been extensively explored across various fields of physics, including high-energy physics, condensed matter physics, and classical wave systems such as light and sound (1, 2). Despite their diversity, noncommutativity lies at the heart of non-Abelian phenomena, rendering the physics of non-Abelian systems more complex and diverse than that of their Abelian counterparts. Examples include the non-Abelian gauge field (3–7), non-Abelian anyons and their statistics for describing the celebrated fractional quantum Hall effect (8–12), and the non-Abelian topological charges in braiding topological structures with multiple entangled bandgaps (13–18). Notably, the presence of non-Abelian anyons in two-dimensional condensed matter systems has garnered increasing interest (8–10, 19–21). When non-Abelian anyons are swapped by intertwining them along world lines, their wave function exchange behavior is represented by a unitary matrix fundamentally different from that of exchanging fermions or bosons (22). These anyons can be encoded with qubits to achieve quantum logic and fault-tolerant topological quantum computing. However, their implementation in quantum systems often depends on the dynamic winding of anyons, which can be challenging to achieve (23–26).

The non-Abelian braiding of degenerate zero modes has been extended to classical wave systems using light and sound as platforms (27–31), emerging as a multimode geometric effect known as the Berry-Wilczek-Zee phase (32, 33), a matrix generalization of the well-known scalar Berry phase. The braiding of multiple states with non-Abelian characteristics, such as the Thouless pumping of flat-band modes, has also been successfully realized in photonics and acoustics (34–36). While the associated noncommutative operations

hold promises for applications involving unitary matrices, such as photonic quantum logic, these braiding operations are fundamentally restricted to adiabatic conditions, which require a sufficiently long distance and thus hinder practical applications. Consequently, compact photonic non-Abelian systems are highly sought after for investigating more intricate non-Abelian phenomena and developing practical applications in photon and light manipulations. Fortunately, there are schemes known as shortcuts to adiabaticity (STA) (37–44) that emulate the same dynamics within a shorter finite time or distance. Initially proposed for nondegenerate systems, these schemes were later generalized to degenerate manifolds (44).

In this work, we theoretically propose and experimentally demonstrate a STA non-Abelian braiding of photonic modes in three-dimensional (3D) silicon photonic chips. The braiding is achieved by imposing cyclic modulation of the hopping amplitudes among integrated silicon waveguides arranged in a trilayer configuration. An STA strategy (37–44) is proposed to identify an evolution pathway in the parameter space of braiding, enabling fast braiding operations and compact devices functioning as Pauli X, Y, and Z gates. Furthermore, by varying the sequence of two distinct STA braiding processes involving three modes, we experimentally observed different outcomes from identical initial states—a hallmark of non-Abelian braiding. Notably, the STA scheme enables the braiding of telecommunication light within a miniaturized footprint of $1.7 \times 24 \ \mu m^2$ per device unit, nearly three orders of magnitude shorter compared to the state-of-the-art laser-written photonic waveguide system (millimeter scale) (29, 31). This work illustrates the potential to explore non-Abelian physics using a fully integrated complementary metal-oxide semiconductor (CMOS)–compatible silicon platform, ensuring versatile on-chip light manipulations and paving the way for compact non-Abelian photonic integrated devices.

RESULTS

Model

We first illustrate the photonic braiding model with two degenerate zero modes. Figure 1A presents the schematics of the STA braiding structure in a trilayered silicon photonic chip, which comprises
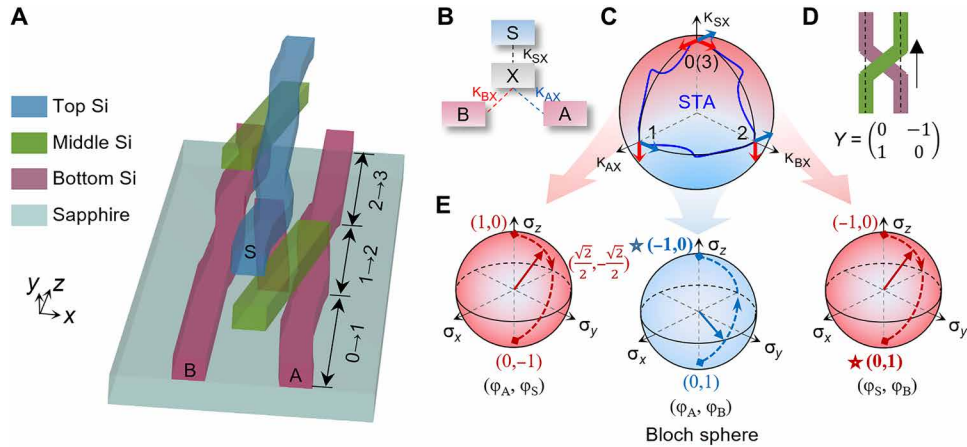
Fig. 1. Braiding on trilayer silicon photonic chips. (**A**) A schematic of the braiding structure consisting of four waveguides implemented in trilayered silicon photonics platform. (**B**) The cross section of the setup in a tight-binding model, including coupling between waveguide X to waveguides A, B, and S, respectively. (**C**) The system sustains two degenerate zero modes, whose parallel transport on the two-sphere exchanges the two modes. The blue trajectory indicates the STA braiding path in the parameter spaces. This process realizes the Y gate, whose braiding diagram is shown in (**D**). (**E**) The zero modes can be mapped onto Bloch spheres of different subspaces for three braiding steps, respectively. The red and blue dashed paths indicate the zero mode evolutions on the Bloch sphere as performing the braiding operations.

three main waveguides (A, B, and S) and an auxiliary waveguide X. The bottom layer includes waveguides A and B (red waveguides) positioned on a sapphire substrate, while the top layer consists of waveguide S (blue waveguide). Waveguide X consists of three disjoint sections as required by the braiding process (to be detailed below). The first and third sections are in the middle layer (green waveguides), whereas the second section (red waveguide) is located in the bottom layer. Waveguides A, B, and S are coupled to waveguide X through evanescent wave coupling κ_{iX} (i = A, B, and S), as indicated by the dashed lines in the cross-sectional view shown in Fig. 1B. The dynamics of photon propagation in the waveguide structure can be described by the following Hamiltonian (*29, 30*)

$$H(z) = \begin{bmatrix} \beta_X & \kappa_{AX}(z) & \kappa_{BX}(z) & \kappa_{SX}(z) \\ \kappa_{AX}(z) & \beta_A & 0 & 0 \\ \kappa_{BX}(z) & 0 & \beta_B & 0 \\ \kappa_{SX}(z) & 0 & 0 & \beta_S \end{bmatrix} \quad (1)$$

where $\beta_{X,A,B,S} = \beta_0$ represents the propagation constant of waveguides, and the coupling coefficient κ_{iX} is set to be real and is a specific function of parameter z (the propagation distance along the waveguides, i.e., the braiding direction, the waveguide length is L). Since all other waveguides must couple through waveguide X, the system can be divided into two groups: one consisting of waveguide X and the other comprising waveguides A, B, and S. Consequently, the Hamiltonian Eq. 1 can be simplified as $H = \begin{pmatrix} \mathbf{0}_1 & \boldsymbol{\kappa}^T \\ \boldsymbol{\kappa} & \mathbf{0}_3 \end{pmatrix}$, where $\mathbf{0}_3$ is an 3×3 zero matrix and $\boldsymbol{\kappa} = (\kappa_{AX}, \kappa_{BX}, \text{ and } \kappa_{SX})^T$ represents the vector space of the three coupling parameters. This Hamiltonian clearly exhibits sublattice symmetry, which ensures the presence of $|3-1| = 2$ degenerate zero modes in this case (note that there are also two splitting modes, which are not the focus of this work). These two zero modes reside within the group of waveguides A, B, and S, forming the braiding subspace. As illustrated in Fig. 1C, the unit hopping vector $\hat{\boldsymbol{\kappa}} = \boldsymbol{\kappa}/|\boldsymbol{\kappa}|$ defines a unit two-sphere, with the two zero modes spanning a tangent plane on this two-sphere (marked by

the red and blue arrows in Fig. 1C). The braiding process consists of three steps (step 0-1, 1-2, and 2-3) and forms a cyclic modulation of z, driving the tangent vectors of zero modes in a holonomic parallel transport. This process encloses a solid angle of $\pi/2$ on the two-sphere and realizes the Y gate $Y = \begin{pmatrix} 0 & -1 \\ 1 & 0 \end{pmatrix}$, a fundamental quantum logic components [U(2) operation] that swaps the two modes as $|\Psi_1\rangle \rightarrow |\Psi_2\rangle$ and $|\Psi_2\rangle \rightarrow -|\Psi_1\rangle$.

Specifically, the system's initial configuration ($z = 0$) is located at the north pole of the parameter space, and it contains two zero modes, occupying waveguides A and B, respectively, i.e., $|\Psi_1(0)\rangle = (0,1,0,0)^T$, $|\Psi_2(0)\rangle = (0,0,1,0)^T$. Here, $|\Psi_i\rangle$ represents a state vector with its elements indicating the wave function in waveguides X, A, B, and S, respectively, i.e., $|\Psi_i\rangle = (\varphi_{Xi}, \varphi_{Ai}, \varphi_{Bi}, \varphi_{Si})^T$. The braiding process consists of three steps, each traversing a distance of $L/3$, as shown in Fig. 1C. In step 0-1 represented by the black arc connecting points 0 and 1, κ_{SX} (κ_{AX}) decreases (increases) from its maximum (zero) to zero (its maximum), while κ_{BX} is kept at zero. The initial state $|\Psi_1(0)\rangle = (0,1,0,0)^T$ becomes $|\Psi_1(L/3)\rangle = (0,0,0,-1)^T$. The zero mode evolutions can be mapped onto a Bloch sphere, where the eigenstates evolve from the north pole to the south pole of the Bloch sphere formed by the subspace (φ_A, φ_S), acquiring a π phase during the evolution (Fig. 1E, left). On the other hand, the initial state in waveguide B $|\Psi_2(0)\rangle$ remains the same, $|\Psi_2(L/3)\rangle = |\Psi_2(0)\rangle = (0,0,1,0)^T$, as $\kappa_{BX} = 0$ during the step 0-1. In step 1-2, the state in waveguide B is transferred to site A with a geometric phase π, i.e., from $|\Psi_2(L/3)\rangle = (0,0,1,0)^T$ to $|\Psi_2(2 L/3)\rangle = (0,-1,0,0)^T$. This corresponds to the zero mode evolution from the south pole to the north pole of the Bloch sphere formed by subspace (φ_A, φ_B) (Fig. 1E, middle). In contrast, the state in waveguide S remains unchanged $|\Psi_1(2 L/3)\rangle = |\Psi_1(L/3)\rangle = (0,0,0,-1)^T$ as $\kappa_{SX} = 0$. In step 2-3, the state in waveguide S transfers to the waveguide B and also acquires the π phase $|\Psi_1(L)\rangle = (0,0,1,0)^T$. Accordingly, the eigenstates evolve from the north pole to the south pole of the Bloch sphere formed by the subspace (φ_S, φ_B) (Fig. 1E, right). On the contrary, the state in waveguide A remains unchanged, i.e., $|\Psi_2(L)\rangle = |\Psi_2(2 L/3)\rangle = (0,-1,0,0)^T$ as $\kappa_{AX} = 0$. Overall, the initial states $|\Psi_1(0)\rangle = (0,1,0,0)^T$

and $|\Psi_2(0)\rangle = (0,0,1,0)^T$ lastly become $|\Psi_1(L)\rangle = (0,0,1,0)^T$ and $|\Psi_2(L)\rangle = (0,-1,0,0)^T$ (marked by the two pentagrams in Fig. 1E), completing the braiding operations and functioning as quantum Y gates.

Notably, the braiding process typically requires adiabatic conditions (*27–31, 34–36*), which necessitate a long operation distance. If the evolutionary distance is simply reduced, then the system parameters will vary rapidly, leading to instantaneous eigenmode coupling and consequently undermining the braiding function. To address this issue, we propose to use STA braiding strategy to accelerate the adiabatic process, thus ensuring the desired state evolutions with a significantly reduced system length, as will be elaborated below.

STA braiding

Transitionless driving, a well-known STA method proposed by Berry (*37*), can inhibit immediate eigenmode coupling caused by rapid parameter variations by incorporating counterdiabatic driving terms (*38–44*). Since the fundamental component of the braiding process is the adiabatic zero-mode evolution within a triplet subsystem, we apply the STA strategy to this basic process and then extend it to the entire braiding procedure. Specifically, we consider the first step (0-1) of the braiding process as a subsystem, as indicated by the dashed box in Fig. 2A, which only involves waveguides A, X, and S. The triplet unit supports a zero mode $|\varphi_0\rangle$ and two split modes $|\varphi_\pm\rangle$, with the corresponding Hamiltonian [in the subspace of $(\varphi_A, \varphi_X, \varphi_S)$]

$$H(z) = \begin{bmatrix} \beta_A & \kappa_{AX}(z) & 0 \\ \kappa_{AX}(z) & \beta_X & \kappa_{SX}(z) \\ 0 & \kappa_{SX}(z) & \beta_S \end{bmatrix} \quad (2)$$
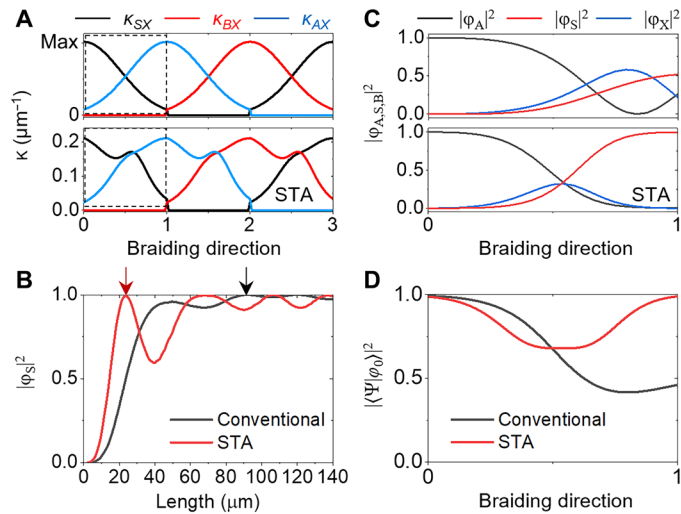

Fig. 2. Design of STA braiding. (**A**) The original modulation profiles of the coupling coefficients (top). The coupling coefficients in STA braiding process (bottom) at the working wavelength $\lambda = 1550$ nm. (**B**) The transferred light intensity $|\varphi_S|^2$ as a function of the length of the subsystem (waveguides A, X, and S). The STA braiding allows complete energy transfer within a short system length 24 μm (marked by red arrow), while the conventional process requires at least 92 μm to allow complete transfer (black arrow). (**C**) Evolution of the light intensity in the subsystem along the braiding direction (step 0-1) during the conventional (top) and STA (bottom) process. (**D**) Zero-mode occupancy $|\langle\Psi|\varphi_0\rangle|^2$ during the braiding process. The evolution length is 24 μm for (C) and (D).

Before applying the STA operation to Eq. 2, we note that this Hamiltonian satisfies the one-photon resonance condition (i.e., $\beta_A = \beta_X = \beta_S$), allowing us to map $H(z)$ to an effective two-level system

$$H_{\text{eff}}(z) = \begin{bmatrix} \kappa_{SX}(z)/2 & \kappa_{AX}(z)/2 \\ \kappa_{AX}(z)/2 & -\kappa_{SX}(z)/2 \end{bmatrix} (39, 42, 43).$$ This premapping prevents the generation of complex or long-range couplings during the STA operations (*39*), thereby enabling a feasible STA braiding system.

Following Berry's protocol (*37*), the counterdiabatic driving term $H_{\text{eff\_CD}}(z)$ of the mapped system has the form

$$H_{\text{eff\_CD}}(z) = i \sum_n \sum_{m \neq n} \frac{|m(z)\rangle \langle m(z)| \frac{\partial}{\partial z} H_{\text{eff}}(z) |n(z)\rangle \langle n(z)|}{E_n(z) - E_m(z)} \quad (3)$$

where $|m>$ and $|n>$ respectively denote eigenstates of the two-level systems with eigenvalues E_m and E_n. Then, the STA Hamiltonian of the effective system can be obtained by adding $H_{\text{eff\_CD}}(z)$ to $H_{\text{eff}}(z)$, i.e.,

$$H_{\text{eff\_STA}}(z) = H_{\text{eff}}(z) + H_{\text{eff\_CD}}(z) = \begin{bmatrix} \tilde{\kappa}_{SX}(z)/2 & \tilde{\kappa}_{AX}(z)/2 \\ \tilde{\kappa}_{AX}(z)/2 & -\tilde{\kappa}_{SX}(z)/2 \end{bmatrix}, \text{ where}$$

$H_{\text{eff\_CD}}(z)$ can inhibit the diabatic eigenmode transfer caused by rapidly changing $H_{\text{eff}}(z)$. Last, the STA version of the original triplet $H_{\text{STA}}(z)$ is obtained by mapping $H_{\text{eff\_STA}}(z)$ back to the triplet subsystem

$$H_{\text{STA}}(z) = \begin{bmatrix} \beta_A & \tilde{\kappa}_{AX}(z) & 0 \\ \tilde{\kappa}_{AX}(z) & \beta_X & \tilde{\kappa}_{SX}(z) \\ 0 & \tilde{\kappa}_{SX}(z) & \beta_S \end{bmatrix} \quad (4)$$

We see that the STA strategy modifies the coupling coefficients in the braiding process, which consequently alters the loop path along the braiding direction on the two-sphere (see blue path in Fig. 1C). This STA Hamiltonian can be achieved by varying waveguides A, S, and X along the propagation direction (see schematics in Fig. 1A). The detailed procedure for performing STA braiding can be found in section S1.

The coupling strength of the conventional adiabatic design [following the stimulated Raman adiabatic passage (*45–47*)] and the STA braiding process are shown in the top and bottom of Fig. 2A, respectively. For the light input from waveguide A, the transferred light intensity to waveguide S $|\varphi_S|^2$ as a function of the length of the subsystem (step 0-1) is shown in Fig. 2B. It is evident that the STA design offers the capability to complete the braiding process within a significantly reduced evolution distance; the minimum length required for the conventional pumping process to achieve complete transfer is 92 μm, while it could be shortened to 24 μm (approximately 3.8 times smaller) for the STA braiding. Specifically, the light evolutions in the STA device and conventional case are shown in Fig. 2C. The STA braiding enables the zero mode to transfer from waveguide A to S within this short distance (24 μm, see Fig. 2C, bottom), while the conventional process only leads to partial transfer at the same distance (see Fig. 2C, top). Further analysis of the zero-mode occupancy during the pumping process reveals that the conventional braiding path results in significant cross-talk between the pumped zero mode and other modes (black curve, Fig. 2D). In contrast, the STA path maintains the dominance of the zero mode, ensuring that even in the presence of cross-talk, it ultimately returns to the zero-energy level (red curve, Fig. 2D), thus successfully fulfilling the braiding operation.

Figure 3 shows the simulated light evolutions during the STA braiding process. The system's initial states ($z = 0$) are two zero
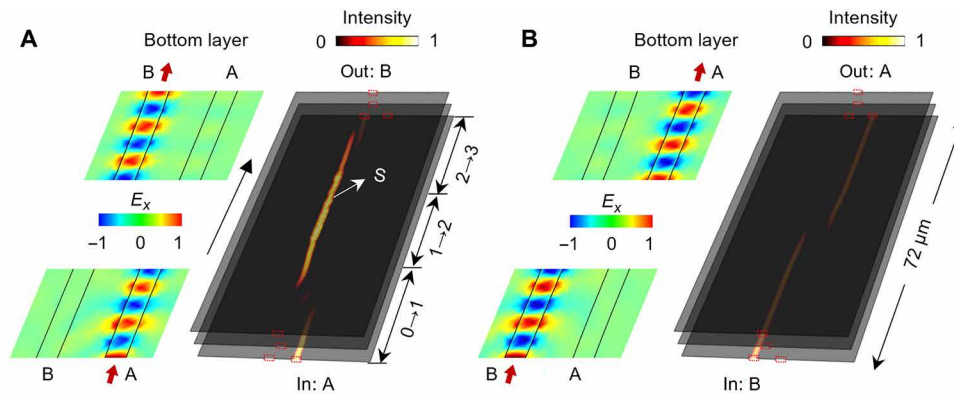
Fig. 3. Numerical study of STA braiding in trilayer silicon waveguides. (**A**) For input from waveguide A. Left: Evolution of E_x field at the input and output ends. Right: Evolution of light intensity in the STA braiding process. The red boxes in the input and output ends mark the position of the waveguides. (**B**) Corresponding results for waveguide B input.

modes occupying waveguides A and B, respectively, i.e., $|\Psi_1(0)\rangle = (0,1,0,0)^T$, $|\Psi_2(0)\rangle = (0,0,1,0)^T$. After the braiding process, both $|\Psi_1\rangle$ and $|\Psi_2\rangle$ undergo energy exchange between waveguides A and B. However, $|\Psi_1\rangle$ follows the A-S-B path without geometric phase inversion (see Fig. 3A, where the input and output have the same phase indicated by the red color), while $|\Psi_2\rangle$ undergoes a single pumping process from B to A (Fig. 3B, where the input and output fields are in red and blue, indicating a phase difference of π). Therefore, the output geometric phase of $|\Psi_2\rangle$ differs from the initial phase by π (the accumulated dynamical phases are both $\beta_0 L$), which is the expected outcome of the Y gate. Following the same STA-braiding principle, the Pauli X and Z gates can also be designed and realized in the trilayer silicon photonic platform (see section S2).

Experimental observations

We fabricated the trilayer-integrated waveguide samples using E-beam lithography with AR-N 7520 resists and an inductively coupled plasma etching process (*48*). The bottom layer waveguides are fabricated in a silicon wafer on a sapphire substrate. A layer of SU-8 with a thickness of 530 nm covering the bottom waveguides is prepared, followed by the coating of a second silicon film with a thickness of about 220 nm, which is further processed to form the second layer waveguides. The third layer of silicon is fabricated following the same procedures (see Materials and Methods for fabrication details).

To clearly observe the fabricated trilayer waveguide structure, we used a focused ion beam to cut holes into the surface of the sample, allowing the cross section of the waveguide sample to be viewed through a scanning electron microscope (SEM), as shown in Fig. 4. Here, Fig. 4 (A to C) illustrates the cross section of the braiding steps 0-1, 1-2, and 2-3, respectively, and the corresponding top panels show the schematics of each cross section. In optical measurements, a laser light ($\lambda = 1550$ nm) was focused into the waveguide lattice through an input grating coupler. The transmitted light, scattered from the extended output ports, can be collected for analysis. Both the coupling-in and coupling-out processes were captured using a near-infrared charge-coupled device (CCD) camera.

Figure 4 (D and E) demonstrates that the two zero modes can switch the light dwelling (A-B and B-A), as required by the braiding process of the Y gate. To further confirm the geometric π phase difference of the two outcomes, two identical Y gate braiding structures (e.g., Y_1 and Y_2) were excited with different input ports (e.g.,

$A_1 B_2$, which means inputs from waveguide A in the Y_1 device and waveguide B in the Y_2 device) or the same ports (e.g., $A_1 A_2$), and their outputs were combined to interfere with each other. As shown in Fig. 4F, the experimental observations confirm that outputs from different input waveguides ($A_1 B_2$) had opposite phases (no light comes from the central port), while outputs from the same input waveguides ($A_1 A_2$) had identical phases (the intensity of the central output is observed to be enhanced), confirming that the braiding device achieved the π geometric phase difference of the Y gate.

Non-Abelian STA braiding

The successful demonstration of the Y gate shows that our STA design and the integrated photonic platform can be extended to obtain the non-Abelian braiding of (N) modes. As a proof of concept, we realized the three-mode non-Abelian braiding operations, representing the minimalist non-Abelian braiding process described by a braid group (B_3) (*29*, *30*), as shown in the schematics in Fig. 5 (A and C). The three-mode STA non-Abelian braiding structure comprises seven waveguides. The three primary waveguides, labeled A, B, and C, are positioned sufficiently far from one another, necessitating coupling through auxiliary waveguides X_1 and X_2, which are individually cut into three parts similar to the two-mode braiding process.

The Hamiltonian of the system supports three degenerate zero modes that constitute the braiding subspace. In this case, exchanging $|\Psi_2\rangle$ and $|\Psi_1\rangle$ is captured by the matrix $G_1 = \begin{pmatrix} Y & 0 \\ 0 & 1 \end{pmatrix}$, and the exchange of $|\Psi_3\rangle$ and $|\Psi_2\rangle$ is given by $G_2 = \begin{pmatrix} 1 & 0 \\ 0 & Y \end{pmatrix}$. Here, $|\Psi_i\rangle$ represents a state vector with its three elements indicating the wave function in waveguides A, B, and C, respectively. It is easy to check that $G_1 G_2 \neq G_2 G_1$, which is a fundamental characteristic that classifies B_3 as a non-Abelian group. The simulation results in Fig. 5 (B and D) shows the evolution of the light field during the three-mode braiding process. When the braiding sequence is $G_2 G_1$, the output light signal sequentially shifts one site to the right. Conversely, the output sequentially shifts one site to the left with the $G_1 G_2$ sequence. The different braiding sequences result in opposite outcomes, verifying the non-Abelian nature of the braiding process. Notably, the STA non-Abelian braiding process is accomplished within 144 μm, nearly three orders of magnitude shorter than the state-of-the-art
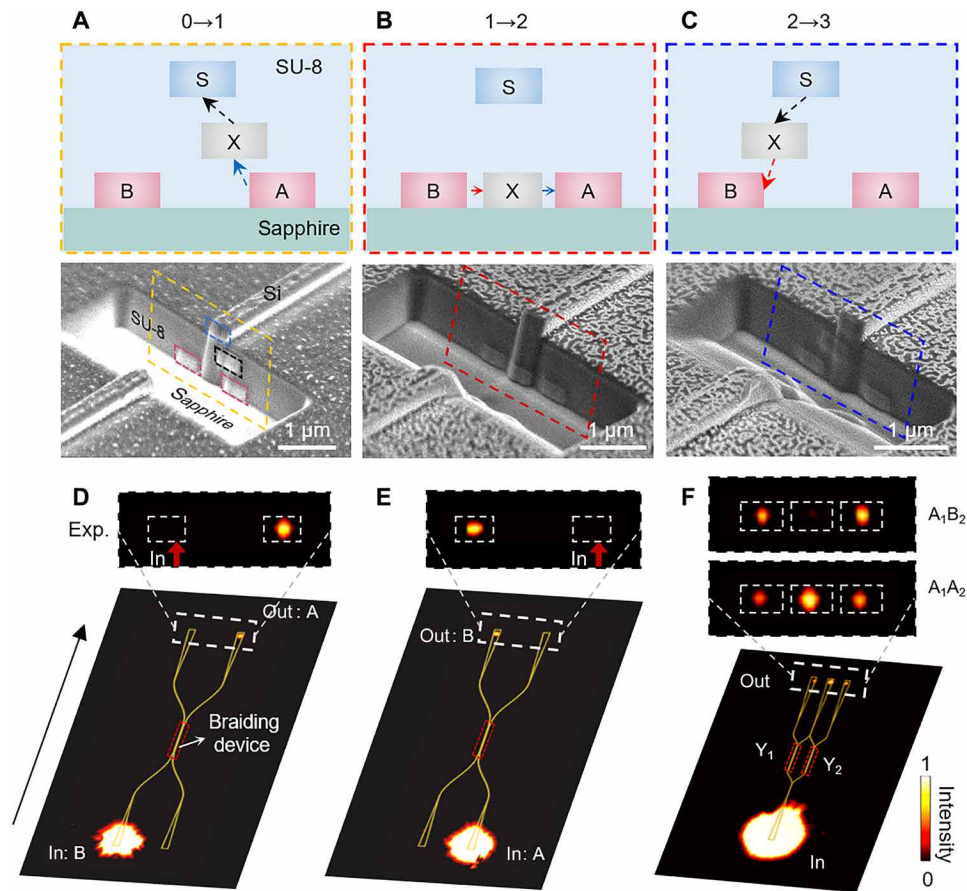
Fig. 4. Experimental implementation of Y gate. (**A** to **C**) Schematics for different stages of the trilayer waveguide systems (top) and SEM images for fabricated samples (bottom). (**D** to **F**) CCD recorded light couple-in and couple-out processes in the braiding samples of (D) waveguide B input, (E) waveguide A input, and (F) double Y gate interference results. The top shows the experimentally captured zoom-in pictures of the output ports. In (F), two identical Y gate structures (Y_1 and Y_2) were input simultaneously, and the interference of their output states reveals the geometric phase. Specifically, the upper output result corresponds to A_1B_2 inputs (i.e., inputs from waveguide A in the Y_1 device and waveguide B in the Y_2 device); while the lower output result corresponds to A_1A_2 inputs.

laser-written photonic waveguide systems, which operate on a millimeter scale (*29*, *31*). It is also ~3.8 times smaller compared to the conventional design on the same silicon platform. This miniaturization could enhance the integration density of non-Abelian photonic chips and minimize the impact of dimensional uncertainties due to nanofabrication, thereby enabling scaling to larger circuits with more complex non-Abelian photonic device networks.

DISCUSSION

In summary, we have achieved STA braiding of photonic modes within 3D silicon photonic chips. Using a trilayer waveguide configuration and applying the STA strategy to the hopping amplitudes, we successfully executed fast zero-mode braiding operations functioning as Pauli X, Y, and Z gates. Further experimental observation of non-Abelian braiding at telecommunication wavelengths underscores the practical applicability of the STA braiding scheme. Compared to previous works (*28*–*31*, *34*–*36*), our results demonstrate the feasibility of realizing non-Abelian devices with significantly reduced sizes, facilitating the construction of quantum logic gates in CMOS-compatible silicon photonics chips. In bosonic systems, a unique feature is that the holonomic dimension scales with the

excitation level (*31*). While the STA braiding demonstrated here uses classical light, it is anticipated that using two-photon inputs in STA braiding schemes would result in higher-dimensional holonomies, enabling more complex non-Abelian optical operations for manipulating photons and light at the micro- and nanoscale.

MATERIALS AND METHODS
Fabrication of the trilayer silicon waveguide samples
The waveguide arrays and grating nanostructures are fabricated using the method of electron-beam lithography and inductively coupled plasma (ICP) etching process. The substrate used herein is 220-nm silicon deposition on an alumina substrate, and the substrates are cleaned in ultrasound bath in acetone and deionized water for 10 min respectively and dried under clean nitrogen flow. Then, a layer of MA-N2405 photoresist film is spin-coated onto the substrate and baked at 90°C for 3 min. After that, the sample is exposed to electron beam in E-beam writer (Elionix, ELS-F125) and developed to form the MA-N2405 nanostructures. Then, the sample is transferred into HSE Series Plasma Etcher 200 and etched with C_4F_8 and SF_6 [the flow rates of these two types of gases are 75 standard cubic centimeter per minute (sccm):30 sccm]. After the ICP
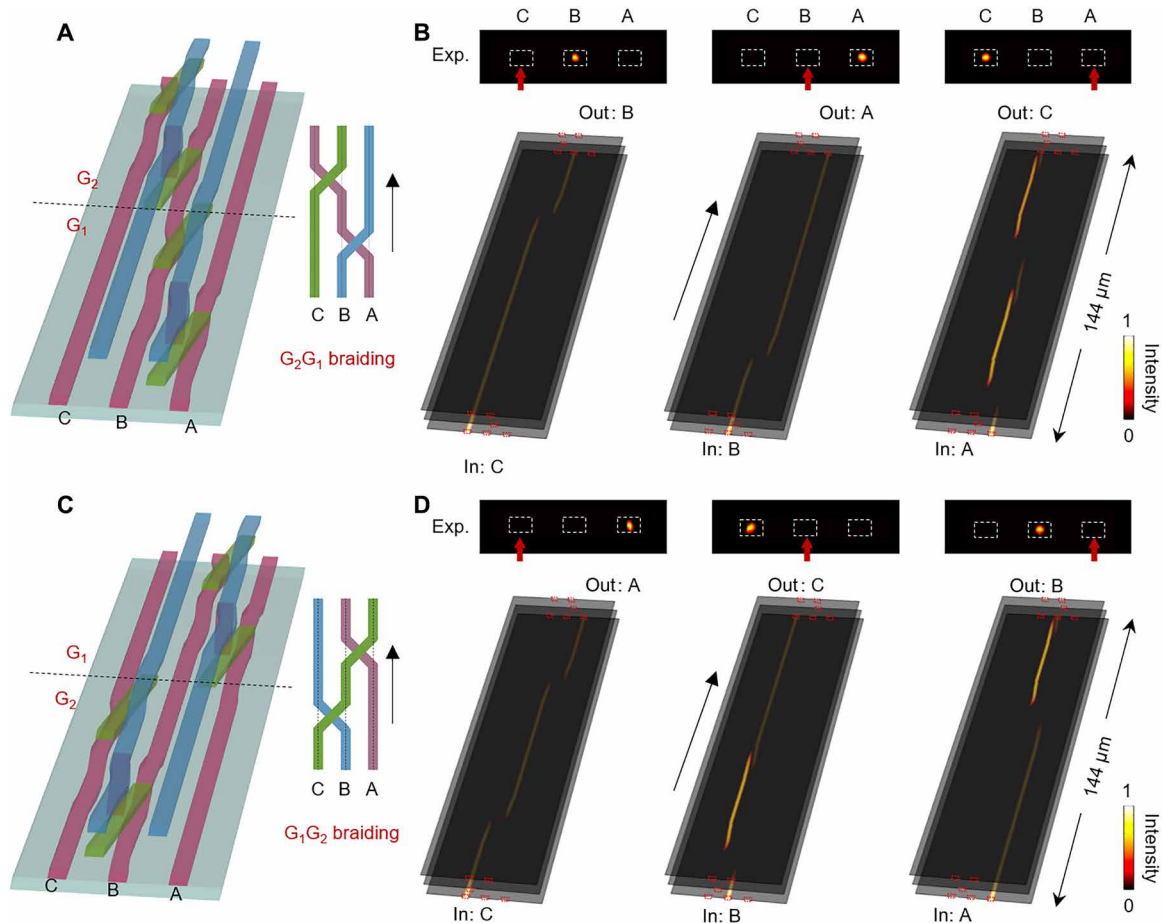
Fig. 5. Experimental observation of STA non-Abelian braiding. (**A**) A schematic of the G_2G_1 braiding structure. (**B**) Simulation (bottom) and experimental (top) results of the G_2G_1 braiding, showing propagation (simulation) and output light field distribution (experiment) from waveguides A, B, and C inputs. The red boxes in the input and output end mark the position of the waveguides. (**C** and **D**) Corresponding results of the G_1G_2 braiding.

etching, the remaining MA-N2405 is removed by using an O_2 plasma for 5 min. Before the fabrication of the second layer of nanostructures, 530-nm SU-8 resist is spin-coated onto the sample and baked at 200°C for 30 min for protection. Then, another α-Si layer was deposited on the SU-8 using the plasma-enhanced chemical vapor deposition to a final thickness of 220 nm. Repeat the above process twice to fabricate the second and third layers afterward (see fig. S3 for the fabrication flow).

Supplementary Materials

This PDF file includes:
Supplementary Text
Figs. S1 to S3
Table S1

REFERENCES AND NOTES

1. Y. Yang, B. Yang, G. Ma, J. Li, S. Zhang, C. T. Chan, Non-Abelian physics in light and sound. *Science* **383**, eadf9621 (2024).
2. Q. Yan, Z. Wang, D. Wang, R. Ma, C. Lu, G. Ma, X. Hu, Q. Gong, Non-Abelian gauge field in optics. *Adv. Opt. Photonics* **15**, 907–976 (2023).
3. T. T. Wu, C. N. Yang, Concept of nonintegrable phase factors and global formulation of gauge fields. *Phys. Rev. D* **12**, 3845–3857 (1975).
4. S. Weinberg, Non-Abelian gauge theories of the strong interactions. *Phys. Rev. Lett.* **31**, 494–497 (1973).
5. Y. Chen, R.-Y. Zhang, Z. Xiong, Z. H. Hang, J. Li, J. Q. Shen, C. T. Chan, Non-Abelian gauge field optics. *Nat. Commun.* **10**, 3125 (2019).
6. Y. Yang, C. Peng, D. Zhu, H. Buljan, J. D. Joannopoulos, B. Zhen, M. Soljačić, Synthesis and observation of non-abelian gauge fields in real space. *Science* **365**, 1021–1025 (2019).
7. Z. Dong, X. Wu, Y. Yang, P. Yu, X. Chen, L. Yuan, Temporal multilayer structures in discrete physical systems towards arbitrary-dimensional non-Abelian Aharonov-Bohm interferences. *Nat. Commun.* **15**, 7392 (2024).
8. M. Iqbal, N. Tantivasadakarn, R. Verresen, S. L. Campbell, J. M. Dreiling, C. Figgatt, J. P. Gaebler, J. Johansen, M. Mills, S. A. Moses, J. M. Pino, A. Ransford, M. Rowe, P. Siegfried, R. P. Stutz, M. Foss-Feig, A. Vishwanath, H. Dreyer, Non-Abelian topological order and anyons on a trapped-ion processor. *Nature* **626**, 505–511 (2024).
9. S. Xu, Z.-Z. Sun, K. Wang, H. Li, Z. Zhu, H. Dong, J. Deng, X. Zhang, J. Chen, Y. Wu, C. Zhang, F. Jin, X. Zhu, Y. Gao, A. Zhang, N. Wang, Y. Zou, Z. Tan, F. Shen, J. Zhong, Z. Bao, W. Li, W. Jiang, L.-W. Yu, Z. Song, P. Zhang, L. Xiang, Q. Guo, Z. Wang, C. Song, H. Wang, D.-L. Deng, Non-Abelian braiding of Fibonacci anyons with a superconducting processor. *Nat. Phys.* **20**, 1469–1475 (2024).
10. C. Nayak, S. H. Simon, A. Stern, M. Freedman, S. Das Sarma, Non-Abelian anyons and topological quantum computation. *Rev. Mod. Phys.* **80**, 1083–1159 (2008).
11. Y.-F. Wang, H. Yao, Z.-C. Gu, C.-D. Gong, D. N. Sheng, Non-Abelian quantum hall effect in topological flat bands. *Phys. Rev. Lett.* **108**, 126805 (2012).
12. C. H. Lee, W. W. Ho, B. Yang, J. Gong, Z. Papić, Floquet mechanism for non-Abelian fractional quantum hall states. *Phys. Rev. Lett.* **121**, 237401 (2018).
13. A. Bouhon, Q. Wu, R.-J. Slager, H. Weng, O. V. Yazyev, T. Bzdušek, Non-Abelian reciprocal braiding of Weyl points and its manifestation in ZrTe. *Nat. Phys.* **16**, 1137–1143 (2020).
14. B. Peng, A. Bouhon, B. Monserrat, R.-J. Slager, Phonons as a platform for non-Abelian braiding and its manifestation in layered silicates. *Nat. Commun.* **13**, 423 (2022).

15. R.-J. Slager, A. Bouhon, F. Nur Ünal, Non-Abelian Floquet braiding and anomalous Dirac string phase in periodically driven systems. *Nat. Commun.* **15**, 1144 (2024).

16. Q. Guo, T. Jiang, R.-Y. Zhang, L. Zhang, Z.-Q. Zhang, B. Yang, S. Zhang, C. T. Chan, Experimental observation of non-Abelian topological charges and edge states. *Nature* **594**, 195–200 (2021).

17. B. Jiang, A. Bouhon, Z.-K. Lin, X. Zhou, B. Hou, F. Li, R.-J. Slager, J.-H. Jiang, Experimental observation of non-Abelian topological acoustic semimetals and their phase transitions. *Nat. Phys.* **17**, 1239–1246 (2021).

18. T. Jiang, Q. Guo, R.-Y. Zhang, Z.-Q. Zhang, B. Yang, C. T. Chan, Four-band non-Abelian topological insulator and its experimental realization. *Nat. Commun.* **12**, 6471 (2021).

19. F. Wilczek, Magnetic flux, angular momentum, and statistics. *Phys. Rev. Lett.* **48**, 1144–1146 (1982).

20. F. Wilczek, Quantum mechanics of fractional-spin particles. *Phys. Rev. Lett.* **49**, 957–959 (1982).

21. E. Witten, Quantum field theory and the Jones polynomial. *Commun. Math. Phys.* **121**, 351–399 (1989).

22. J. M. Leinaas, J. Myrheim, On the theory of identical particles. *Nuovo Ciment. B* **37**, 1–23 (1977).

23. S. Das Sarma, M. Freedman, C. Nayak, Topologically protected qubits from a possible non-Abelian fractional quantum Hall state. *Phys. Rev. Lett.* **94**, 166802 (2005).

24. M. Freedman, C. Nayak, K. Walker, Towards universal topological quantum computation in the ν = 5/2 fractional quantum Hall state. *Phys. Rev. B* **73**, 245307 (2006).

25. M. Freedman, A. Kitaev, M. Larsen, Z. Wang, Topological quantum computation. *Bull. Am. Math. Soc.* **40**, 31–38 (2003).

26. A. Kitaev, Fault-tolerant quantum computation by anyons. *Ann. Phys.* **303**, 2–30 (2003).

27. T. Iadecola, T. Schuster, C. Chamon, Non-Abelian braiding of light. *Phys. Rev. Lett.* **117**, 073901 (2016).

28. J. Noh, T. Schuster, T. Iadecola, S. Huang, M. Wang, K. P. Chen, C. Chamon, M. C. Rechtsman, Braiding photonic topological zero modes. *Nat. Phys.* **16**, 989–993 (2020).

29. X.-L. Zhang, F. Yu, Z.-G. Chen, Z.-N. Tian, Q.-D. Chen, H.-B. Sun, G. Ma, Non-Abelian braiding on photonic chips. *Nat. Photon.* **16**, 390–395 (2022).

30. Z.-G. Chen, R.-Y. Zhang, C. T. Chan, G. Ma, Classical non-Abelian braiding of acoustic modes. *Nat. Phys.* **18**, 179–184 (2022).

31. V. Neef, J. Pinske, F. Klauck, L. Teuber, M. Kremer, M. Ehrhardt, M. Heinrich, S. Scheel, A. Szameit, Three-dimensional non-Abelian quantum holonomy. *Nat. Phys.* **19**, 30–34 (2023).

32. M. V. Berry, Quantal phase factors accompanying adiabatic changes. *Proc. R. Soc. Lond. A Math. Phys. Sci.* **392**, 45–57 (1984).

33. F. Wilczek, A. Zee, Appearance of gauge structure in simple dynamical systems. *Phys. Rev. Lett.* **52**, 2111–2114 (1984).

34. V. Brosco, L. Pilozzi, R. Fazio, C. Conti, Non-Abelian Thouless pumping in a photonic lattice. *Phys. Rev. A* **103**, 063518 (2021).

35. Y.-K. Sun, X.-L. Zhang, F. Yu, Z.-N. Tian, Q.-D. Chen, H.-B. Sun, Non-Abelian Thouless pumping in photonic waveguides. *Nat. Phys.* **18**, 1080–1085 (2022).

36. O. You, S. Liang, B. Xie, W. Gao, W. Ye, J. Zhu, S. Zhang, Observation of Non-Abelian Thouless pump. *Phys. Rev. Lett.* **128**, 244302 (2022).

37. M. V. Berry, Transitionless quantum driving. *J. Phys. A Math. Theor.* **42**, 365303 (2009).

38. Y.-X. Du, Z.-T. Liang, Y.-C. Li, X.-X. Yue, Q.-X. Lv, W. Huang, X. Chen, H. Yan, S.-L. Zhu, Experimental realization of stimulated Raman shortcut-to-adiabatic passage with cold atoms. *Nat. Commun.* **7**, 12479 (2016).

39. Y.-C. Li, X. Chen, Shortcut to adiabatic population transfer in quantum three-level systems: Effective two-level problems and feasible counterdiabatic driving. *Phys. Rev. A* **94**, 063411 (2016).

40. D. Guéry-Odelin, A. Ruschhaupt, A. Kiely, E. Torrontegui, S. Martínez-Garaot, J. G. Muga, Shortcuts to adiabaticity: Concepts, methods, and applications. *Rev. Mod. Phys.* **91**, 045001 (2019).

41. W. Huang, Y. Chen, X. Qu, S. Yin, X. Shi, X. Xiong, W. Zhang, Z. Qin, Y. Zhang, Complete and robust light transfer in three-waveguide coupler by shortcut to adiabaticity. *AIP Adv.* **10**, 095104 (2020).

42. A. K. Taras, A. Tuniz, M. A. Bajwa, V. Ng, J. M. Dawes, C. G. Poulton, C. Martijn De Sterke, Shortcuts to adiabaticity in waveguide couplers–theory and implementation. *Adv. Phys. X* **6**, 1894978 (2021).

43. S. Wu, W. Song, J. Sun, Z. Lin, H. Xin, S. Zhu, T. Li, Broadband asymmetric light transport in compact lithium niobate waveguides. *Laser Photon. Rev.* **17**, 2300306 (2023).

44. T. Karzig, F. Pientka, G. Refael, F. von Oppen, Shortcuts to non-Abelian braiding. *Phys. Rev. B* **91**, 201102(R) (2015).

45. N. V. Vitanov, A. A. Rangelov, B. W. Shore, K. Bergmann, Stimulated Raman adiabatic passage in physics, chemistry, and beyond. *Rev. Mod. Phys.* **89**, 015006 (2017).

46. S. Longhi, G. Della Valle, M. Ornigotti, P. Laporta, Coherent tunneling by adiabatic passage in an optical waveguide system. *Phys. Rev. B* **76**, 201101(R) (2007).

47. R. Menchon-Enrich, A. Llobera, J. Vila-Planas, V. J. Cadarso, J. Mompart, V. Ahufinger, Light spectral filtering based on spatial adiabatic passage. *Light Sci. Appl.* **2**, e90 (2013).

48. W. Song, O. You, J. Sun, S. Wu, C. Chen, C. Huang, K. Qiu, S. Zhu, S. Zhang, T. Li, Fast topological pumps via quantum metric engineering on photonic chips. *Sci. Adv.* **10**, eadn5028 (2024).